

# Deep Learning Methods for Calibrated Photometric Stereo and Beyond: A Survey

Yakun Ju, Kin-Man Lam, Wuyuan Xie, Huiyu Zhou, Junyu Dong, and Boxin Shi

**Abstract**—Photometric stereo recovers the surface normals of an object from multiple images with varying shading cues, *i.e.*, modeling the relationship between surface orientation and intensity at each pixel. Photometric stereo prevails in superior per-pixel resolution and fine reconstruction details. However, it is a complicated problem because of the non-linear relationship caused by non-Lambertian surface reflectance. Recently, various deep learning methods have shown a powerful ability in the context of photometric stereo against non-Lambertian surfaces. This paper provides a comprehensive review of existing deep learning-based calibrated photometric stereo methods. We first analyze these methods from different perspectives, including input processing, supervision, and network architecture. We summarize the performance of deep learning photometric stereo models on the most widely-used benchmark data set. This demonstrates the advanced performance of deep learning-based photometric stereo methods. Finally, we give suggestions and propose future research trends based on the limitations of existing models.

**Index Terms**—Photometric stereo, deep learning, non-Lambertian, surface normals.

## 1 INTRODUCTION

ACQUIRING three-dimensional (3D) geometry from two-dimensional (2D) scenes is a fundamental problem in computer vision. It aims to establish computational models that allow computers to perceive the external 3D world. Unlike geometric approaches (such as multi-view stereo and binocular) that use different viewpoint scenes to compute 3D points, photometric stereo [16] perceives the 3D shape of an object from varying shading cues observed under different lighting conditions with a fixed viewpoint. Compared to geometric methods that generally reconstruct rough shapes, photometric methods can acquire more detailed local reconstruction, as shown in Fig. 1. Therefore, photometric stereo plays a mainstream role in many high-precision 3D reconstruction tasks, such as cultural relic reconstruction [3], seabed mapping [4], moon surface reconstruction [5], and industrial defect detection [6], *etc.*

Classic photometric stereo [16] assumes that only the Lambertian (diffuse) reflectance exists on the surface of the target object. Under the Lambertian assumption, the surface normal can be easily solved by the least squares method, because the reflection intensity  $M$  is linearly proportional to the angle between the normal  $n$  and incident light  $l$ , as follows:

$$M \propto l^\top n. \quad (1)$$

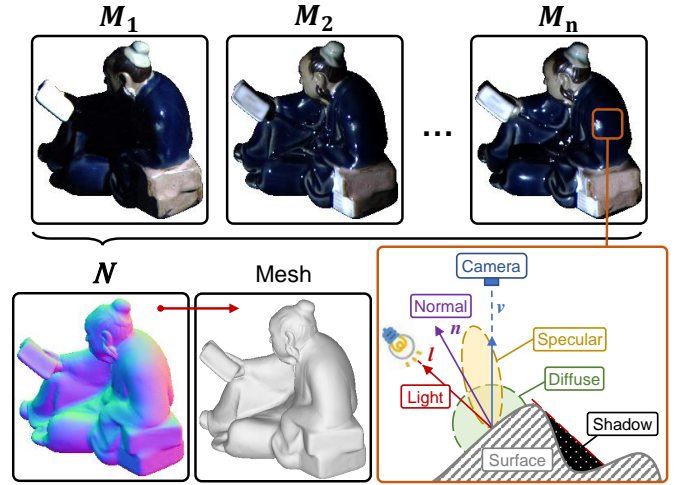


Fig. 1. Photometric stereo methods obtain detailed shape reconstructions from multiple images under different illuminations. The orange box shows the general surface reflectance. In this survey, we take the object “Reading” from the DiLiGenT benchmark [25] as visual example, which has spatially varying and non-Lambertian materials with strong specularity and shadow.

However, real-world objects only barely have the property of Lambertian reflectance. The non-Lambertian property of surfaces (as shown in the orange box in Fig. 1) affects the proportional relationship of Eq. 1. Mathematically, we express the non-Lambertian property via the bidirectional reflectance distribution function (BRDF), depending on the material of the object. According to the previous taxonomies [25], [27], [57], plenty of work has addressed non-Lambertian photometric stereo by modeling BRDF [18], [19], [29], rejecting outlier regions [20], [21], [68], or setting exemplars [30], [31]. However, these non-learning models are only accurate for limited materials and suffer from unstable optimization.

- Y. Ju and K.M. Lam are with the Department of Electronic and Information Engineering, The Hong Kong Polytechnic University, Hong Kong (e-mail: kelvin.yakun.ju@gmail.com, enklam@polyu.edu.hk).
- W. Xie is with the Research Institute for Future Media Computing, Shenzhen University, Shenzhen, China (e-mail: wuyuan.xie@gmail.com).
- H. Zhou is with the Department of Informatics, University of Leicester, Leicester, UK (e-mail: hz143@leicester.ac.uk).
- J. Dong is with the School of Computer Science and Technology, Ocean University of China, Qingdao (e-mail: dongjunyu@ouc.edu.cn).
- B. Shi is with the National Engineering Research Center of Visual Technology, School of Computer Science, Peking University, Beijing, China (e-mail: shiboxin@pku.edu.cn).

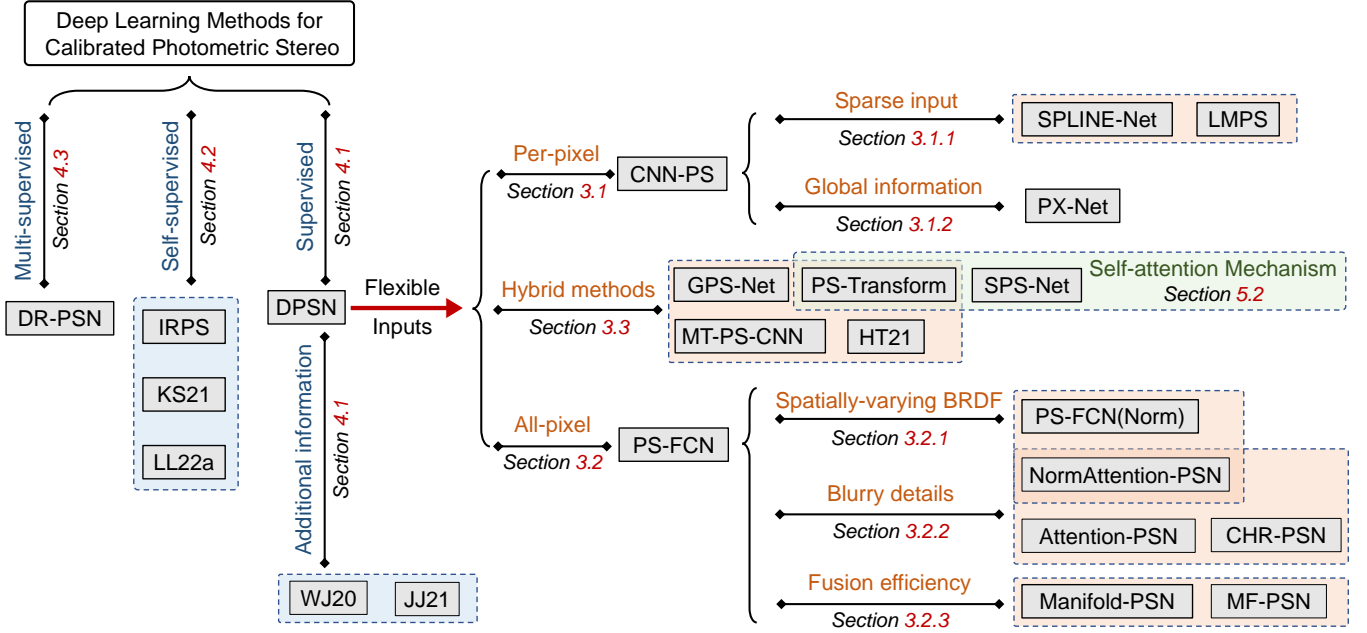


Fig. 2. Overview of deep learning methods for calibrated photometric stereo. These methods are further tabulated in Table 3 for detailed comparison.

In fact, artificial neural networks have been introduced in the context of photometric stereo over the past three decades [1], [2], [7]. However, these models are restricted to limited materials that lack practical applications or require pre-training with a reference object with the same material as the target. Recently, deep learning techniques have shown potential power in various fields of computer vision. In 2017, modern deep neural networks emerged in photometric stereo starting with DPSN [22]. DPSN [22] first showed superior performance on non-Lambertian surfaces compared with traditional hand-crafted models. However, this method requires fixed illumination directions during training and testing, which limits its generalization. Furthermore, the used fully-connected network handles a single surface point and inevitably ignores the information embedded in the neighborhood.

To address the aforementioned problems, various deep learning-based methods have been proposed. Ikehata [32] proposed the observation map to record an arbitrary number of intensities with arbitrary light directions, which improves the generalization of the model. On the other hand, Chen *et al.* [23] introduced max-pooling to handle an arbitrary number of input images. With the recent summary [8], these learning-based methods can be categorized according to how they process the input images, as per-pixel methods (*i.e.*, by the observation map operation [32] to record the intensity of each pixel) or all-pixel methods (*i.e.*, by using max-pooling [23] to fuse whole patches). However, the previous survey [8] only considered five calibrated learning-based photometric stereo models for these two methods, which also lacks a comprehensive summary and discussion of the pros and cons of the methods and how they were developed. Many models were then proposed along with the per-pixel approach [9], [33], [34] or the all-pixel approach [10], [11], [36], [47]. Some of the methods combine these two approaches and take full advantage

of them [12], [42]. Therefore, it is necessary to propose a more complete taxonomy to summarize these methods and discuss future research directions for deep learning-based photometric stereo. In this survey, we first comprehensively summarize the development of the per-pixel and all-pixel methods, following the taxonomy [8], and then propose a new classification named hybrid methods.

Furthermore, categorizing these methods, based only on how they process input images, is not sufficient. In this paper, we further analyze the literature from the perspective of supervision, *i.e.*, how the methods optimize the network (Section 4). Most deep photometric stereo networks are trained with paired photometric stereo images (input) and surface normals (ground truths), *i.e.*, supervised learning. Whether a photometric stereo network can be optimized in a self-supervised way? Whether additional information can be added to simplify the learning of surface-normal recovery? On these sides, this paper reviews recent attempts to expand and break through the supervised frameworks [13], [35], [37], [43] and gives suggestions for future developments.

Meanwhile, with the development of GPUs, the complexity and number of parameters of learning-based models increase dramatically. The suitable deep architectures and training data sets influence the performance of the model potentially. It can be seen that many advanced modules have been used for the surface-normal recovery task, including ResNet [38], DenseNet [14], HR-Net [48], Transformer [60], *etc.* Similarly, those synthetic training data sets face a selection, *i.e.*, rendering with MERL BRDF [40] or Disney's principled BSDF [15]. In this paper, we compare and discuss the network architectures (Section 5) and data sets (Section 6) that have been employed for previous deep learning-based photometric stereo.

According to the above-mentioned classifications, we first survey the previous calibrated deep learning photo-

TABLE 1  
Summary of calibrated deep learning photometric stereo algorithms and formulations.

They predict surface normals $N$ or $\mathbf{n}_p$ from input photometric images $M^i$ or pixel $m_p^i$ and its light direction $l^i$ , where $p$ stands for the index of spatial resolution $H \times W$ , $i \in \{1, 2, \dots, n\}$ stands for the index of inputs. $f$ represents deep neural networks for learning surface normals (Eq. 3).		
Sec.	DPSN [22]	$\mathbf{n}_p = f(\bar{m}_p^i)$ , where $\bar{m}_p^i$ means the order and the number of the inputs are fixed.
3.1	CNN-PS [32]	$\mathbf{n}_p = f(\text{obs}(m_p^i, l^i))$ , please see obs in Section 3.1.
3.1.1	SPLINE-Net [34]	$\mathbf{n}_p = f(D(\text{obs}(m_p^i, l^i)))$ , where $D$ stands for the Lighting Interpolation Network.
3.1.2	PX-Net [9]	$\mathbf{n}_p = f(\text{obs}(G(m_p^i), l^i))$ , where $G$ stands for the global illumination effects.
3.2	PS-FCN [23]	$N = f_R(\max\{f_E(M^i, l^i)\})$ , please see max in Section 3.2, $f_E$ and $f_R$ mean the Extractor and Regressor.
3.2.1	PS-FCN (Norm.) [47]	$N = f_R(\max\{f_E(\text{norm}(\sum_i^n M^i), l^i)\})$ , where norm stands for the Observation Normalization.
3.2.2	Attention-PSN [36]	$N = f_R(\max\{f_E(M^i, l^i)\})$ , with minimizing the adaptive loss $\mathcal{L} = \lambda \mathcal{L}_{\text{gradient}} + (1 - \lambda) \mathcal{L}_{\text{normal}}$ .
3.2.3	MF-PSN [10]	$N = f_R(\max_d\{\max_s\{f_E(M^i, l^i)\}, f_E(M^i, l^i)\})$ , where $s$ and $d$ mean shallow and deep, respectively.
3.3	GPS-Net [42]	$N = f(\cup_p^{H \times W} \text{gcn}(m_p^i, l^i))$ , where gcn stands for the Structure-aware Graph Convolution filters.
4.3	DR-PSN [43]	$N = f_P(M^i, l^i) = f_I^{-1}(M^i)$ , where $f_P$ and $f_I$ mean the PhotometricNet and Image RenderingNet.
4.2	IRPS [35]	$N = f_P(M^i) = f_I^{-1}(M^i)$ , with minimizing the self-supervised loss $\mathcal{L} = f_I(f_P(M^i), l^i) - M^i$ .
4.1.1	WJ20 [37]	$\mathbf{n}_p = f_R(\max\{f_E(m_p^i, l^i, m_p^0)\})$ , where $m_p^0$ stands for the collocated light observation.
5.2	PS-Transform [62]	$N = f_R(f_E(m_p^i, l^i), f_E(M^i))$ , where $f_E$ and $f_R$ are layers with the Self-attention Mechanism.

metric stereo methods. An overview of the calibrated deep learning-based photometric stereo methods is shown in Fig. 2. As tabulated in Table 1, we further summarize the algorithms of representative methods for each direction in Fig. 2. Then, we evaluate more than 30 deep learning models for photometric stereo on the widely used benchmark [25] in dense input condition (Table 3) and sparse input condition (Table 4), respectively. Compared with traditional non-learning methods, deep learning-based photometric stereo models are superior in estimating surface normals. Finally, we point out the future trends in the field of photometric stereo. We hope that this survey will help researchers to understand the state-of-the-art methods and position themselves to develop in this growing field, as well as highlighting opportunities in the future research.

## 2 PROBLEM FORMULATION

Consider a pixel on a non-Lambertian surface with the normal  $\mathbf{n}$  illuminated by a parallel incident light  $\mathbf{l}$ . When a linear-response camera photographs this surface in the view direction  $\mathbf{v}$ , the pixel-measured intensity  $m$  in image  $M$  can be approximated as follows:

$$m = \rho(\mathbf{n}, \mathbf{l}, \mathbf{v}) \cdot \max\{\mathbf{n}^\top \mathbf{l}, 0\} + \epsilon, \quad (2)$$

where  $\rho$  represents the BRDF, and  $\max\{\mathbf{n}^\top \mathbf{l}, 0\}$  denotes the attached shadows, and  $\epsilon$  is an error term representing the impacts, such as cast shadows and inter-reflections [26], that are difficult to be described by the BRDF. Traditional photometric stereo methods compute the surface normals of general objects by solving the imaging model Eq. 2 inversely, using more than three input images, but unknown BRDFs make the model difficult to fit (as shown in Fig. 1). Similarly, deep learning-based calibrated photometric stereo methods aim to learn a neural network model  $f$  as follows:

$$f : \sum_i^n (M^i, l^i) \rightarrow N, \quad (3)$$

where  $f$  is the optimized deep neural network by the training data sets. Note that the model  $f$  becomes  $f : \sum_i^n M^i \rightarrow N$  when addressing uncalibrated photometric stereo.

In the following subsections, we will discuss these deep learning-based photometric stereo methods from different perspectives.

## 3 CATEGORIZATION BASED ON INPUT PROCESSING

The first deep learning method, DPSN [22], makes the order of illuminations and the number of input images unchanged, by a seven-layer fully-connected network. Therefore, the following methods focus on handling any number of input images with arbitrary light directions. In fact, this problem is equivalent to how to fuse a varying number of features in the networks. It is known that convolutional neural networks (CNNs) cannot handle a varying number of inputs during training and testing. Therefore, two approaches have been proposed in photometric stereo, *i.e.*, to process the input images pixel-wise or patch-wise. Following the concept proposed in [8], we also call the pixel-wise and patch-wise processing methods as per-pixel methods (Section 3.1) and all-pixel methods (Section 3.2), respectively. We provide an in-depth summary of the development of these two approaches, in reference to the drawbacks of the initial methods (*i.e.*, the observation map from CNN-PS [32] and the max-pooling from PS-FCN [23]). In addition, we propose a new class, for hybrid methods (Section 3.3), which fuse pixel- and patch-wise characteristics.

### 3.1 Per-pixel methods

The per-pixel strategy is first realized by the observation map in CNN-PS [32]. The observation map merges all observations pixel-by-pixel (extract the inter-image intensity variation of each pixel [81]). As shown in Fig. 3, the fusion rule is based on the pixel intensity and the orthogonal projected light direction. Specifically, this approach aggregates the respective pixels of each input image into a fixed-size

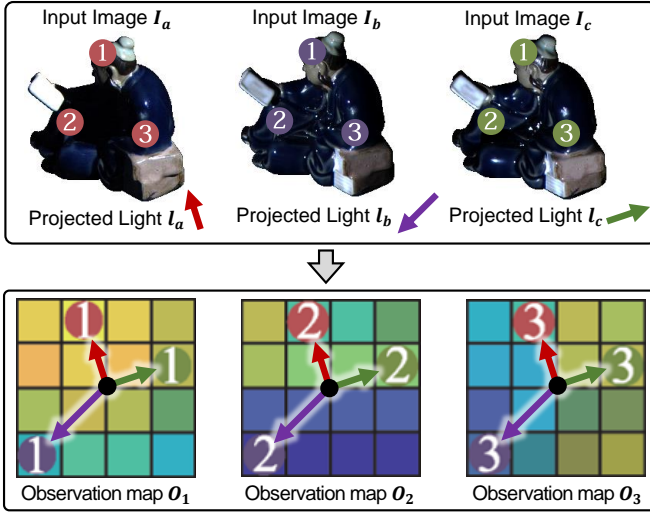


Fig. 3. Observation maps [32] are determined by projecting light directions from a 3D space (hemisphere) onto a plane. Each observation map can represent the feature at a single-pixel position. Here, a, b, and c stand for the number of input images (lights), while 1, 2, and 3 stand for the index of pixel position.

observation map by the 2D coordinates of projected normalized lighting directions (along axis- $z$ ). The observation map is effective in the photometric stereo task because of three reasons. First, its size is independent of the number of input images. Second, its values are independent of the order of the input images. Third, the information of the lighting directions is embedded in the observation map [32].

### 3.1.1 Problem of sparse input

However, the observation map also encountered some problems. First, light directions are represented by unstructured vectors, while observation maps are grid data as images. When projecting a light vector onto a 2D coordinate system, the projected direction can not exactly correspond to the grid observation map. To improve the accuracy of projected light directions, the size of the observation map has to be large enough to approximately represent the unstructured projected vectors. Unfortunately, the number of input images (light directions) is sparse compared to the size of the observation map, which creates difficulties in extracting features. In fact, the sparse observation map affects network performance. As shown in Fig. 4, the accuracy of CNN-PS drops significantly when inputting a small number of images (sparse condition), compared with the all-pixel method PS-FCN [23] and the least squares method [16].

In this regard, some works were proposed to solve the sparse input images problem, such as SPLINE-Net [34] and LMPS [33]. In fact, these two methods adopt opposite strategies to solve this problem. SPLINE-Net [34] proposed a lighting interpolation network to generate dense lighting observation maps when the input is sparse (as shown in Fig. 5(a)). To optimize the lighting interpolation network and normal estimation network, SPLINE-Net [34] further utilizes a symmetric loss and an asymmetric loss to consider general BRDF properties explicitly and outlier rejections, respectively. On the other hand, LMPS [33] attempted to reduce the demands on the number of images by only

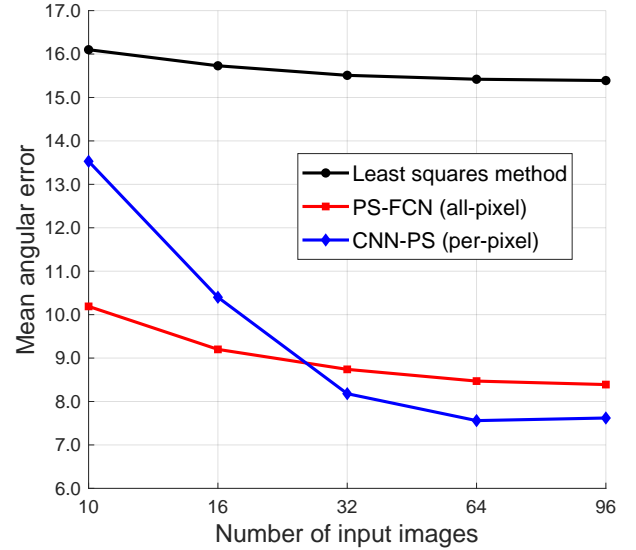


Fig. 4. Comparison of different numbers of input images, with the least squares method [16], the all-pixel method PS-FCN [23], and the per-pixel method CNN-PS [32].

learning the critical illumination conditions. The method employs a connection table to select those illumination directions that are the most relevant to the surface normal prediction process (as shown in Fig. 5(b)). Furthermore, a more thorough method [42] is to replace the structured observation map with an unstructured graph network, which will be introduced in Section 3.3.

### 3.1.2 Problem of global information

The second problem is that these methods isolate the spatial constraints within intra-image. The observation map only represents a single position in the whole image. However, this mechanism ignores the information embedded in the neighborhood of a surface point, which cannot make full use of the input images.

Due to “isolated” processing in per-pixel methods, their robustness is worse than that of the all-pixel methods. For example, the first 20 images of the object “Bear” in the DiLi-GenT benchmark data set [25] are corrupted: the intensity values around the bear’s stomach region are lower than the adjacent regions, although they should be higher because of the specularities [32]. When all the 96 images of “Bear” are input into CNN-PS [32], the mean angular error increases dramatically, from 4.20 (with the first 20 images discarded) to 8.30, an increase of 97.62%. In contrast, all-pixel methods are much more robust, *e.g.*, PS-FCN [23], the error increased from 5.02 to 7.55, by 50.40% only, and NormAttention-PSN [50], the error increased from 4.80 to 5.48, by 14.17% only. The lesser robustness of the per-pixel methods can be seen when encountering wrong illuminations. This problem also causes the performance of CNN-PS [32] to degrade when increasing the number of input images from 64 to 96 (as shown in Fig. 4, the blue line increases slightly from 64 to 96).

To solve this problem, some recent works incorporated global information into observation map-based per-pixel methods, which lead to superior performance, such as PX-



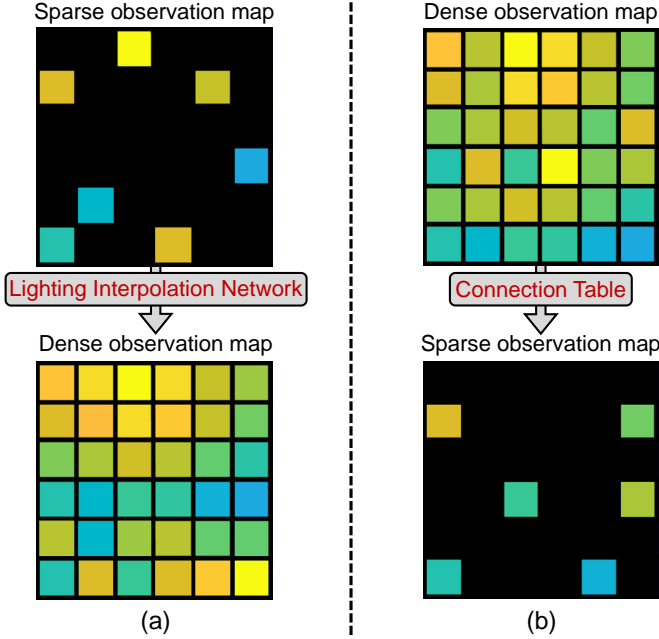


Fig. 5. Per-pixel methods for sparse input images. (a) Diagram showing the lighting interpolation network to generate dense observation maps, used in SPLINE-Net [34]. (b) Diagram showing the connection table used to select the most relevant illuminant directions in the sparse observation maps, used in LMPS [33].

Net [9]. PX-Net [9] proposed an observation map-based method that considers global illumination effects, such as self-reflections, surface discontinuity, and ambient light, which enables global information to be embedded in the per-pixel generation process. Other methods, such as HT21 [12] and GPS-Net [42], learn global information (intra-image features) by combining the per-pixel and all-pixel strategies. We will discuss these methods in Section 3.3.

### 3.2 All-pixel methods

Different from per-pixel methods separately handling each pixel in observations, all-pixel methods keep all the pixels together. All-pixel methods can explore intra-image intensity variations across a whole input image but pay less attention to inter-image shading variations under different illuminations. The original all-pixel method was proposed in PS-FCN [23], implemented by a max-pooling layer, which works on the channel dimension to fuse an arbitrary number of features, *i.e.*, each position on the fused feature is the maximum value of all input features at that position. Therefore, the method can make a convolutional network to handle the fused feature from an arbitrary number of inputs. The max-pooling layer is inspired by aggregating multi-image information in computer vision tasks [49], [51]. Compared with the variable input method RNN [52], the adopted max-pooling operation, as an order-agnostic method, is not sensitive to the light order of the input. The all-pixel max-pooling operation is also effective for photometric stereo. First, it can handle an arbitrary number and order-free input images. Second, the features of the whole image contain local context information, which benefits the estimation of surface normals. Third, the patch-based input makes the

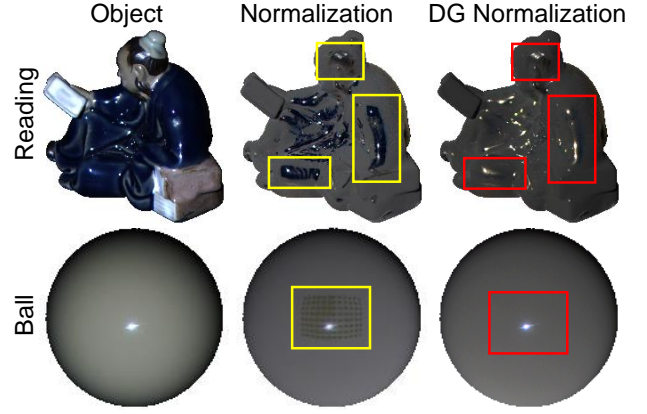


Fig. 6. Comparison of the original normalization method [47] and the double-gate normalization method [50]. DG stands for double-gate. The yellow boxes represent the suppressed regions, while the red boxes show the results of the normalization without suppression.

training process faster than per-pixel methods. Fourth, all-pixel methods separately handle the input images and light directions (as extra information). Therefore, these models can predict photometric stereo with unknown illuminations (uncalibrated photometric stereo).

#### 3.2.1 Problem of spatially varying BRDF

However, the original all-pixel method PS-FCN [23] has some drawbacks. First, PS-FCN cannot handle surfaces with spatially varying materials. Since all-pixel methods leverage convolutional networks to process input in a patch-based manner, they may have difficulties in dealing with steep color changes caused by surfaces with spatially varying materials. It can be seen as the negative effect of considering observations in the neighborhood when computing the feature maps.

To solve this problem, Chen *et al.* further proposed PS-FCN (Norm.) [47]. Rather than creating a large-scale training set with spatially-varying materials, an observation normalization method, which concatenates all the observations and normalizes them, was introduced, as follows:

$$m'_i = \frac{m_i}{\sqrt{m_1^2 + \dots + m_n^2}}, \quad i \in \{1, 2, \dots, n\}, \quad (4)$$

where  $m_i$  and  $m'_i$  represent the original and normalized pixel intensities in the  $n$  images. Under the assumption of Lambertian reflectance, the effect of albedo can be removed. However, PS-FCN (Norm.) [47] cannot perfectly handle the condition of non-Lambertian surfaces. Because for regions with specular highlights, the observations under other light directions will be suppressed after normalization [47], as shown in the yellow boxes in Fig. 6. Although max-pooling can naturally ignore non-activated features, the suppressed observations are not equal to the suppressed features, *i.e.*, the changing appearance of an observation may cause larger feature values. Therefore, Ju *et al.* [50] proposed a double-gate observation normalization to better handle the non-Lambertian surfaces with spatially-varying materials. In the method, two gates are set at the lowest 10% ( $P_{10}$ ) and the

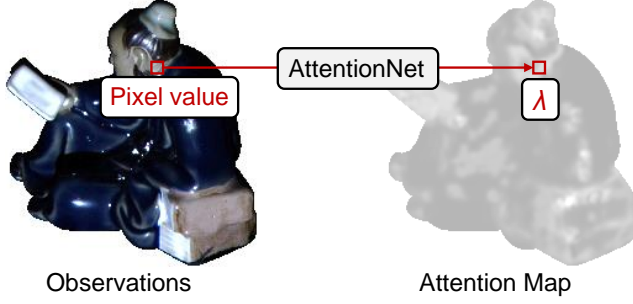


Fig. 7. An example of an attention map from Attention-PSN [36].  $\lambda$  is the weight of the pixel-wise attention-weighted loss (Eq. 6).

highest 10% ( $P_{90}$ ) grayscale values of all pixels and put it on the denominator of Eq. 4, as follows:

$$m'_i = \frac{m_i}{\sqrt{\sum_k m_k^2}}, k \in \mathcal{S}, \quad (5)$$

where the set  $\mathcal{S}$  is controlled by the two gates, such that  $m_i \in \mathcal{S}$  if  $Gate(P_{10}) < m_i < Gate(P_{90})$ , for  $i = 1, 2, \dots, n$ . It can be seen that the non-Lambertian effects are removed in the red boxes in Fig. 6. However, this method has to concatenate with the original images, since discarding some grayscale values in the denominator can be viewed as a nonlinear process, which may affect the shading cues for photometric stereo [50].

### 3.2.2 Problem of blurry details

The second problem with all-pixel methods is that they may cause blurred reconstructions in complex-structured regions. We believe that the reasons mainly lie in three. (1) The convolutional models process patch-based input, which means that all normal points will mutually affect each other and cause blurring, especially in high-frequency areas. (2) The widely used Euclidean-based loss functions can hardly constrain the high-frequency (*i.e.*, complex-structured) representations, because of the “regression-to-the-mean” problem [53], which results in blurry and over-smoothed images. (3) Previous network architectures pass the input through high-low-high resolutions, *i.e.*, through an encoder-decoder architecture, which leads to the loss of prediction details and causes blurring.

In this regard, two different strategies are proposed to deal with the problem of blurred reconstruction in all-pixel methods. The first approach is to employ adaptive loss for different kinds of surfaces. Attention-PSN [36] is the first to propose an attention-weighted loss to produce detailed reconstructions, as follows:

$$\mathcal{L} = \lambda \mathcal{L}_{\text{gradient}} + (1 - \lambda) \mathcal{L}_{\text{normal}}, \quad (6)$$

which learns a higher weight for the detail-preserving gradient loss  $\mathcal{L}_{\text{gradient}}$  and a lower weight for the cosine loss  $\mathcal{L}_{\text{normal}}$  for high-frequency regions. As shown in Fig. 7, Attention-PSN [36] learns an attention map from input images, whose pixel values become the weights of the attention-weighted loss. However, the surface materials of an object may change rapidly in a flat or smooth region, which affects the gradient loss with a large weight in the region and dilutes the penalty on surface normals. Therefore,

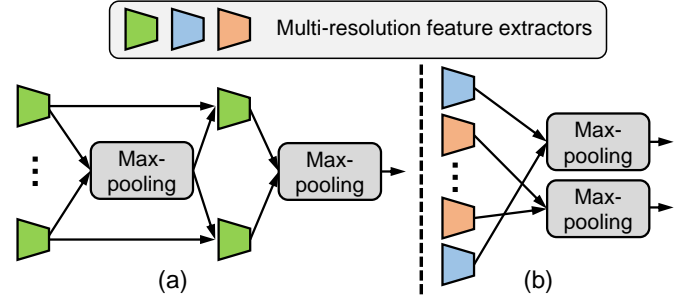


Fig. 8. All-pixel methods for better fusion. (a) Schematic of MF-PSN [10] that uses shallow and deep max-pooling operations in the network. (b) Schematic of CHR-PSN [11] that uses max-pooling operations in multi-resolution features.

Ju *et al.* further employed the above double-gate observation normalization to eliminate the influence of spatially-varying surface materials, namely NormAttention-PSN [50]. On the other hand, the second approach is to preserve the high-resolution features via novel network architectures. With this approach, CHR-PSN [11] proposes a parallel network structure for maintaining both deep features and high-resolution details of surface normals, inspired by the High-resolution Net (HR-Net) [48] for human pose estimation. Full-resolution features can always be preserved in the network, avoiding features passing layers from high to low resolution and blurring.

### 3.2.3 Problem of fusion efficiency

The third is that the fusion mechanism of all-pixel methods, *i.e.*, max-pooling, discards a large number of features from the input, reducing the utilization of information and affecting the estimation accuracy. Therefore, how to retain more features with key information is essential. Some methods [42], [54] fuse max-pooling and average pooling via a concatenation operation. However, the improvement of adding average-pooling is limited because averaging features may smooth out saliency and dilute valuable features. Different from adding averaging information, Manifold-PSN [44] attempts to introduce nonlinear dimensionality reduction [90] to convert features from high-dimensional feature spaces to low-dimensional manifolds. This can better extract embedded structural information of multiple features. However, the manifold method truncates the backpropagation of the network. Therefore, the authors have to use the max-pooling layer to pre-train the extractor of the network, which is cumbersome and inefficient. On the other hand, MF-PSN [10] proposes a multi-feature fusion network, which uses the max-pooling operation in both shallow and deep layers with different levels of features, to learn richer information. Similarly, CHR-PSN [11] expand max-pooling at different scales with different receptive fields, rather than the depth, as in [10]. We summarize the schematic diagrams of MF-PSN [10] and CHR-PSN [11] in Fig. 8. Although these networks outperform previous methods, none of them can solve the fusion problem of information loss, *i.e.*, the max-pooling layer.

Recently, the Transformer architecture [60] is also used to fuse and communicate features from different input images. PS-Transform [62] first uses a multi-head attention pooling

[89] to fuse an arbitrary number of input features. In this way, the number of elements in a set was shrunk from an arbitrary dimension to one, by giving a learnable query  $Q$  rather than only retaining the maximum value. Multi-head attention pooling [89] can be seen as a global fusion method that considers all feature distributions, instead of only retaining the maximum value.

### 3.3 Hybrid methods

As discussed above, both per-pixel and all-pixel methods have their advantages and drawbacks. All in all, per-pixel methods pay more attention to the modeling of general BRDF while ignoring the global information. In contrast, all-pixel methods are good at recovering areas with shadows and inter-reflections, but are limited in non-uniform materials and high-frequency structures. The future trend is to combine these two strategies to achieve better normal-surface reconstruction.

In fact, the first mixed method can be found in learning-based multispectral photometric stereo [45], which first estimates a coarse surface normal map and then refines it by using the per-pixel method, *i.e.*, a fully connected network. Recently, MT-PS-CNN [55] proposes a two-stage photometric stereo model to construct inter-frame (per-pixel) and intra-frame (all-pixel) representations. Honzatko *et al.* [12] build upon the observation maps but incorporate spatial information using 2D and 4D separable convolutions to better capture global effects. In addition, PS-Transformer [62] designs a dual-branch feature extractor based on the self-attention mechanism [60] to explore pixel- and image-wise features. However, GPS-Net [42] introduces a structure-aware graph convolutional network [88], instead of using observation maps. In GPS-Net, the authors utilize a graph structure to connect an arbitrary number of observations per pixel, avoiding the problem of sparse observation maps [32], and then use convolutional layers to explore spatial information. Therefore, GPS-Net unifies per-pixel and all-pixel processing, thus keeping both inter-image and intra-image information. These hybrid methods can take full advantage of per-pixel and all-pixel approaches, resulting in better performance. As shown in Fig. 9, we summarize the hybrid strategy of HT21 [12] and GPS-Net [42].

However, all existing mixed methods extract per-pixel features and all-pixel features sequentially and independently. We believe that future research should concentrate on better combining these two types of features and how to take the learning process as a whole instead of two separate stages.

## 4 CATEGORIZATION BY SUPERVISION

As a mapping task, conventional learning-based photometric stereo methods optimize the network by minimizing the distance between predicted surface normals and ground-truth surface normals [22], [23], [32], supervised by pairs of photometric stereo images and their surface normals. However, learning-based 3D tasks face challenges due to the difficulties in acquiring and aligning a large number of ground truths. To solve this issue, some researchers have investigated self-supervised learning in photometric stereo

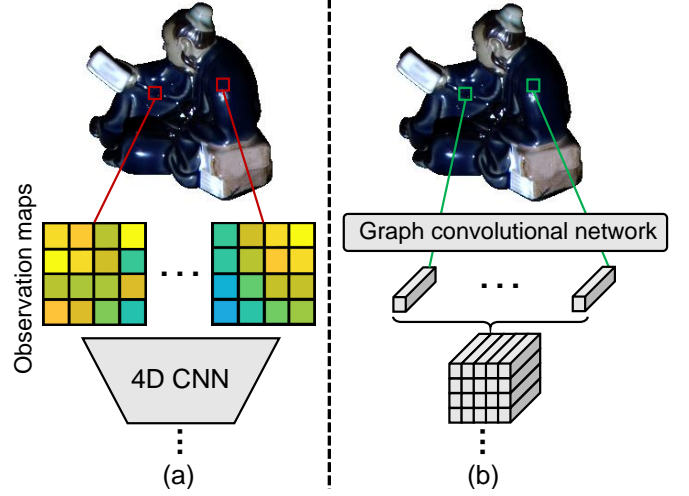


Fig. 9. Hybrid methods for handling both per-pixel features and all-pixel features. (a) Schematic of the 4D CNN to capture the global effect of the observation maps used in HT21 [12]. (b) Schematic of the structure-aware Graph Convolutional network to extract a fixed-size feature map, used in GPS-Net [42].

[35], [56], [59]. Besides, many works further improve the performance by introducing additional supervision [43] or additional information to simplify optimization [13], [37]. In Fig. 10, we summarize the differences among supervised, self-supervised, and multi-supervised photometric stereo networks.

### 4.1 Supervised photometric stereo methods

Plenty of deep photometric stereo networks have been proposed with improved performance, compared to traditional handcrafted photometric stereo methods. These learning-based models show the potential ability of deep neural networks with supervised optimization, *i.e.*, a large amount of data with ground-truth surface normals during the training stage. Among these supervised models, some methods [22], [32], [33], [57] utilize the L2 loss (*i.e.*, mean squared error loss), as follows:

$$\mathcal{L} = \|\mathbf{n}_p - \tilde{\mathbf{n}}_p\|_2^2, \quad (7)$$

while more methods apply cosine similarity loss, as follows:

$$\mathcal{L} = 1 - \mathbf{n}_p \odot \tilde{\mathbf{n}}_p, \quad (8)$$

where  $\odot$  represents the dot-product operation. In this case,  $\mathbf{n}_p \odot \tilde{\mathbf{n}}_p$  will be close to 1 when the predicted  $\tilde{\mathbf{n}}_p$  is similar to the ground truth  $\mathbf{n}_p$ , and Eq. (8) will approach 0. Intuitively, the cosine similarity loss is more suitable for surface-normal estimation, because it directly measures the difference in orientation between two vectors. However, no evidence from previous work shows that L2 loss reduces the accuracy of estimated surface normals with the same network architecture and settings.

#### 4.1.1 Additional information

Recently, some supervised photometric stereo networks have attempted to improve performance with additional information to make optimization more efficient [13], [37]. Wang *et al.* [37] proposed a non-Lambertian photometric

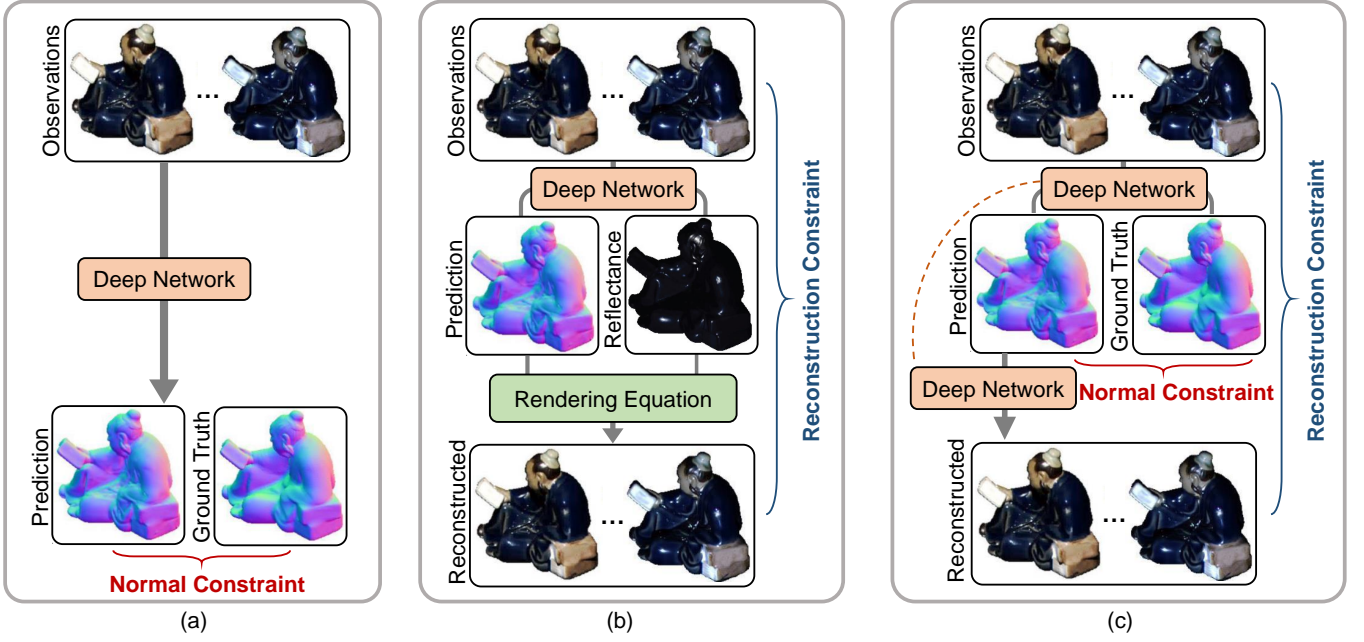


Fig. 10. Comparison of (a) supervised photometric stereo, (b) self-supervised photometric stereo, and (c) multi-supervised photometric stereo.

stereo network with a collocated light. This model can be seen as decoupling surface normals from the monotonicity of isotropic reflectance and the univariate property of the collocated light. In this way, the model is equivalent to using an additional collocated light image to map surface normal, in addition to the input photometric stereo images. Similarly, Ju *et al.* [13] incorporate initial normal priors to better predict surface normals of objects. It utilizes Lambertian assumption information [16] to reparameterize network weights and the powerful fitting ability of deep neural networks to correct these errors caused by general reflectance properties [13]. These methods can achieve better performance by adding extra information to simplify optimization.

In general, supervised photometric stereo methods can achieve superior performance, but these methods are limited due to the difficulties in acquiring accurate ground truth for the real-photoed training sets. Although synthetic images can be used to train models, collecting a large-scale synthetic data set is still impractical, and there is a gap between real photos images and synthetic images due to rendering techniques.

## 4.2 Self-supervised photometric stereo methods

As discussed above, deep learning techniques have drastically advanced the photometric stereo task. Current existing deep learning methods usually solve the problem in a supervised training manner. These methods rely on a large amount of training data with ground truth. However, measuring the surface normals of real objects is very difficult and expensive, because it needs high-precision 3D scanners to reconstruct the ground-truth shape, and requires much manpower to align the viewpoints between surface normal maps and multiple images (pixel alignment). Until now, only two real-world scene data sets have been proposed

[25], [58]. However, these data sets only contain 10 to 100 object scenes and are far from being utilized for training a modern deep neural network. Synthetic training data is a possible way [22], [23], [32], but synthetic images should account for various realistic BRDF, object shapes, cast shadows, and inter-reflections, *etc.* Existing BRDF databases [15], [40] and renderers still require efforts to generate photo-realistic synthetic images.

To overcome the above shortcomings, some researchers have introduced the self-supervised learning strategy, which only needs photometric stereo images, rather than pairs with ground truth surface normals [35], [56], [59]. Tani and Maehara [35] first proposed a self-supervised convolutional network that takes the whole set of images as input, namely IRPS. The model directly outputs surface normals by minimizing the reconstruction loss between observed and re-rendered images, rather than minimizing the distance between predicted and ground truth surface normals. Furthermore, IRPS [35] avoids the unfixed number of input photometric images through its physics-based rendering approach. However, IRPS suffers from expensive computation [8] and fails to model inter-reflections. Moreover, its loss function is not robust and is susceptible to noise and outliers [56] because the surface normals are initialized by using the Lambertian assumption [16]. Therefore, IRPS was further extended by Kaya *et al.* [56] to deal with inter-reflection by explicitly modeling the concave and convex parts of a complex surface. However, both [35], [56] implicitly encode the specular components as features of the network and fail to consider shadows in the rendering process. To solve the limitations, Li *et al.* [59] proposed a coordinate-based deep network to parameterize the unknown surface normal and the unknown reflectance at every surface point. The method learns a series of neural specular basis functions to fit the observed specularities and explicitly parameterizes shadowed regions by tracing the estimated depth map.



However, the method may fail in the presence of strong inter-reflections.

In summary, self-supervised photometric stereo models relax the requirement of massive 3D data sets. We believe that the future directions of self-supervised photometric stereo are to develop more accurate rendering equations, generate more desirable reconstructed images, and improve the effective convergence of reconstructed loss.

### 4.3 Multi-supervised photometric stereo methods

Previous works [13], [37] have shown improved performance with adding input information in supervised learning frameworks. Adding more supervision is another strategy to simplify the learning process. In this paper, we call the methods using multiple supervision “Multi-supervised”. Along these lines, Ju *et al.* [44] proposed a dual regression network for calibrated photometric stereo, namely DR-PSN, which combines the surface-normal constraint and reconstructed image constraint. The authors utilize an inverse subnetwork to re-render reconstructed images from predicted surface normals. Compared with self-supervised learning methods [35], [56], [59], DR-PSN uses the CNN to render reconstructed images rather than conventional rendering equation and does not discard the supervision from surface-normal ground truths. However, DR-PSN suffers from unstable optimization and is limited to fixed surface reflectance rendering, which needs the reflectance feature from the first-stage normal estimate network (as shown in the dotted line of Fig. 10 (c)). Possible future work can explore additional supervision in learning and breaking the limitation of the same surface reflectance between observations and reconstructed images.

## 5 NETWORK ARCHITECTURES

With the development of deep learning techniques, deep learning-based photometric stereo networks have used many advanced modules. In this Section, we will review these modules and compare their advantages and drawbacks in the task of surface normal recovery.

### 5.1 Convolutional networks

In the beginning, DPSN [22] and [57] utilize Multilayer Perceptron (*i.e.*, fully connected layers) with dropout layers to map the surface normals from observations pixel by pixel. However, this architecture ignores adjacent information and cannot handle a flexible number of input images. Therefore, PS-FCN [23] and CNN-PS [32] are proposed to handle an arbitrary number of input images by different strategies (max-pooling and observation map). PS-FCN [23] applies a fully convolutional plain network to learn surface normals, while CNN-PS [32] uses a variant of the DenseNet architecture [14] to estimate surface normals from an observation map. The DenseNet architecture [14] has been widely used in subsequent networks, such as LMPS [33], SPLINE-Net [34], MF-PSN [10], and PX-Net [9], due to its excellent feature extraction capacity. Similarly, ResNet [38] has also been widely used in deep learning-based photometric stereo methods [13], [36], [42], [44], which can effectively avoid gradient vanishing in deep networks. However, the above

structures ignore keeping the high resolution of the features, *i.e.*, passing the features sequentially from high-to-low resolution layers, and then increasing the resolution. This operation is suitable for a high-level task that needs semantic features. However, it may cause information loss and blurring for the per-pixel prediction photometric stereo task. Therefore, some works [11], [50] introduce a parallel multi-scale structure, inspired by the improvement of HR-Net [48] in the human pose estimation task. HR-Net [48] employs a parallel network structure to extract features at three scales, avoiding the feature map being changed from low resolution to high resolution, where the feature extraction process maintains both the deep features with high semantic and high-resolution features having details for surface-normal prediction.

### 5.2 Self-attention mechanism

Transformer with a self-attention module [60] was first proposed in the field of natural language processing. It has also been widely used in many computer vision tasks, where self-attention is employed in the spatial dimensions to capture non-local feature dependencies, which are difficult to be extracted by convolution kernels. Recently, two works [61], [62] also introduce the self-attention mechanism to aggregate features under different lights in the context of photometric stereo. SPS-Net [61] is the first to propose a self-attention photometric stereo network, which aggregates photometric information through a self-attention mechanism. Ikehata *et al.* [62] then presented PS-Transformer, which uses the self-attention mechanism to capture complex interactions in sparse photometric stereo. PS-Transformer [62] designed a dual branch to explore pixel and image-wise features. Therefore, intra-image spatial features and inter-image photometric features are better extracted than with SPS-Net [61].

#### 5.2.1 Discussion

However, can the photometric stereo task take full advantage of the self-attention module? Compared to other computer vision fields that the Transformer module greatly improves the performance [63], [64], but photometric stereo methods with Transformer seem to meet some limitations. First, the Transformer module has greater modeling flexibility and can focus on the information at any position. Therefore, compared with convolutional networks, Transformer requires larger-scale data sets for training. However, the number of samples in existing photometric stereo data sets may fail to support this. Second, the task of photometric stereo usually focuses on recovering the shape of an object instead of a large scene. Moreover, the surface normal of a point only depends theoretically on itself, rather than on its relationship with other long-distance points. In this case, we always use traditional convolutional layers to learn the embedded local context information (*e.g.*, the surface smoothness prior [23]). Therefore, non-local dependence, *i.e.*, Transformer module, may not play a key role in learning the surface-normal feature of objects. Fortunately, the effectiveness of Transformer [62], [79] can be found in an arbitrary number of features communication and features aggregation (by multi-head attention pooling [89]).

TABLE 2  
Summary of data sets for deep learning photometric stereo.

Data set	BRDF	Ground Truth	Number of Sample	Trained methods
Blobby and Sculpture [23]	MERL [40], homogeneous	Synthetic normal	85212	[13], [23], [33], [36], [44], [47], [55] [10], [11], [37], [42], [43], [50], [61]
CyclePS [32]	Disney [15], spatially-varying		45 (75 in [62])	[9], [12], [32], [34], [62]
Gourd & Apple [17]	Real object, spatially-varying	Not provide	3	Test sets
Light Stage Data Gallery [28]			9	
DiLiGenT [25]		3D scanner	10	
DiLiGenT10 <sup>2</sup> [58]	Real object, homogeneous	CAD + CNC	100	

## 6 DATA SETS OF PHOTOMETRIC STEREO

The training and testing of supervised photometric stereo networks require the ground truth normal maps of objects. However, obtaining ground-truth normal maps of real objects is a difficult and time-consuming task. Although many data sets have been established in other 3D reconstruction tasks [65], [66], [67], most of their objects are simple in reflectance and shape, and the number of different lighting conditions is small [25]. This section will review data sets for deep learning-based photometric stereo methods and summarize them in Table 2. It is worth noting that we mainly review these data sets for parallel lighting photometric stereo methods. Those for multiview photometric stereo [86], near-field photometric stereo [87], and multispectral photometric stereo [80] are not discussed here.

### 6.1 Training data sets

Training a deep photometric stereo network needs to render plenty of materials, geometries, and illumination. Researchers have to establish synthetic training data set by rendering 3D shapes with different reflectance. There are two mainstream data sets.

#### 6.1.1 Blobby and Sculpture data set

The first one, the Blobby and Sculpture data set, is proposed in DPSN [22] and improved in PS-FCN [23]. PS-FCN applies 3D shape models from the Blobby shape data set [39] and the Sculpture shape data set [49], as well as the MERL BRDF data set [40] to provide surface reflectance. The Blobby shape data set contains ten objects with various shapes. The Sculpture shape data set [49] further provides more complex (detailed) normal distributions for rendering. The MERL BRDF data set [40] contains 100 different BRDFs with real-world materials, which can provide a diverse set of surface materials for rendering shapes. The authors use a physically based ray tracer, Mitsuba [41] to render photometric stereo images. For each selected shape in these two shape data sets [39], [49], the authors of PS-FCN [23] used 1296 regularly-sampled views, randomly selected 2 of the 100 BRDFs in the MERL BRDF data set, and 64 light directions randomly sampled from the upper hemisphere space to render 64 photometric stereo images with a (cropped) spatial resolution of  $128 \times 128$ . The total number of training samples for the first method is 85212.

#### 6.1.2 CyclesPS data set

The second one is proposed in CNN-PS [32], namely the CyclesPS data set. In this data set, the authors utilize Disney’s

principled BSDF data set [15] rather than the MERL BRDF data set [40] to provide surface reflectance. Compared to the MERL BRDF data set [40], which has 100 measured BRDFs and thus cannot cover the tremendous real-world materials, Disney’s principled BSDF data set integrates five different BRDFs controlled by 11 parameters, which can represent a wide variety of real-world materials. Although CyclesPS data set neglects some combinations of parameters that are unrealistic or do not strongly affect the rendering results, the Disney’s principled BSDF data set can represent almost infinite surface reflectance. The number of 3D model shapes is 15, selected from the Internet under a royalty-free license. The CyclesPS data set [32] uses the Cycles renderer, bundled in Blender [69], to simulate complex light transport. The CyclesPS data set includes three subsets, diffuse, specular, and metallic. Therefore, the total number of samples for training is 45. Different from PS-FCN [23], it divides the object region in the rendered image into 5000 superpixels and uses the same set of parameters at the pixels within a superpixel, *i.e.*, 5000 kinds of materials in one sample. Moreover, the number of light directions is 740, which means that 740 photometric stereo images are rendered for each sample, with a spatial resolution of  $256 \times 256$ . The number of objects in the CyclesPS data set is further increased to 25 in PS-Transformer [62], with the same settings.

#### 6.1.3 Discussion

Compared these two data sets, we can find that the strategy and attention are quite different. As summarized in Table 2, the Blobby and Sculpture data set [23] contains much more samples than the CyclePS data set [32] (85212 vs. 45). However, the number of illuminated images with homogeneous reflectance is 64 in the Blobby and Sculpture data set [23], while there are more than 700 very densely illuminated images with spatially varying materials in the CyclePS data set [32]. The Blobby and Sculpture data set [23] is more suitable for all-pixel methods (see Section 3.2), and the CyclePS data set [32] is better to be used by per-pixel methods (see Section 3.1). There are two reasons. First, all-pixel methods process input images in a patch-wise manner. In contrast, per-pixel methods use the observation map to learn the feature of a single pixel. Therefore, the number of samples is irrelevant as long as the spatial resolution is large enough. Second, before the introduction of the observation strategy [47], all-pixel methods with patch-based inputs cannot handle objects with spatially varying materials, while per-pixel methods naturally avoid this problem. Therefore, previous per-pixel methods usually choose the CyclePS data

set [32] to optimize their models, while all-pixel methods always use the Blobby and Sculpture data set [23] (Tabulated in Table 2). However, the diversity of CyclePS [32] is much better due to the powerful representation ability of the Disney’s principled BSDF data set [15], which can potentially lead to better performance of per-pixel methods using the observation maps strategy. Thus, establishing a Disney’s principled BSDF [15] based on a data set with more samples is important and urgent in future work.

## 6.2 Testing data sets

Test data sets are also needed to quantitatively evaluate the performance of different photometric stereo methods. These data sets can be divided into two categories: synthetic data sets and real-photoed data sets.

### 6.2.1 Synthetic data sets

Synthetic data sets are usually rendered with the same settings as the Blobby and Sculpture data set [23] or the CyclePS data set [32]. For example, the rendered objects “Bunny”, “Dragon”, and “Armadillo” in the Stanford 3D dataset [70] by the MERL BRDF data set [40] as well as the rendered objects “Sphere”, “Turtle”, “Paperbowl”, “Queen”, and “Pumpkin” by the Disney’s principled BSDF data set [15].

### 6.2.2 Real-photoed data sets

To effectively evaluate the robustness and performance of the presented photometric stereo methods, a better choice is to evaluate these methods on real-photoed photometric stereo images rather than synthetic images. Some data sets, such as the Gourd & Apple data set [17] and Light Stage Data Gallery [28], have been proposed for over a decade. The Gourd & Apple data set [17] consists of three objects, namely “Apple”, “Gourd1”, and “Gourd2”, with 112, 102 and 98 images, respectively. The Light Stage Data Gallery [28] consists of six objects, and 253 images are provided for each object. However, these data sets only provide calibrated light directions without ground-truth normal maps. Therefore, one can only qualitatively compare methods on these real-photoed data sets.

To quantitatively evaluate photometric stereo methods, Shi *et al.* [25] first establish a real-photoed photometric stereo data set with ground truth, namely DiLiGenT, which is the most widely used benchmark in the field of photometric stereo. It contains ten objects, ranging from a simple sphere to complicated and concave geometry, with materials ranging from mostly diffuse to strongly non-Lambertian and spatially varying surfaces. The authors illuminated and captured 96 images for each object under different lighting directions. To obtain the ground truth, the authors use a structured light-based Rexcan CS scanner, synchronized with a turn table to acquire 3D point clouds, which can calculate surface normals. Then, the shape-to-image alignment is performed to transform the 3D shape from the scanner coordinate system to the photometric stereo image coordinate system using the mutual information method in Meshlab [71]. Furthermore, the DiLiGenT benchmark [25] provides a test set, which is from a different viewpoint of these photoed objects (except for the object “Ball”) using the same

lighting setup. However, using a small number of objects (10) of DiLiGenT [25] is prone to overfitting in training deep neural networks, and the shapes scanned by a 3D scanner may have errors and blurring. Therefore, Ren *et al.* [58] further proposed a new real-world photometric stereo data set with ground-truth normal maps, namely DiLiGenT10<sup>2</sup> because it contains 10 times larger (one hundred objects of ten shapes multiplied by ten materials) than the widely used DiLiGenT benchmark [25]. The authors used ten shapes to fabricate objects, from CAD models with selected materials, through a high-precise computer numerical control (CNC) machining process, rather than scanning existing objects, which greatly avoids measurement errors. For each shape made, ten materials were used to make the objects, from isotropic (diffuse and specular), anisotropic, to translucent reflectance. The presented training and test data sets for deep learning photometric stereo methods are summarized in Table 2.

## 7 BENCHMARK EVALUATION RESULTS

The evaluation metric is based on the statistics of angular errors. For the whole normal map, the mean angular error (MAE) is calculated as follows:

$$\text{MAE} = \frac{1}{T} \sum_p^T \cos^{-1}(\mathbf{n}_p^\top \tilde{\mathbf{n}}_p), \quad (9)$$

where  $T$  is the total number of pixels on the object, excluding the pixels at background positions, and  $\mathbf{n}_p$  and  $\tilde{\mathbf{n}}_p$  are the ground-truth and estimated surface normal vector at the position indexed  $p$ . In addition to MAE, some papers also use the ratios of the number of surface normals with angular error smaller than  $x^\circ$ , denoted as  $\text{err}_{<x^\circ}$  [36], [50].

In Table 3, we report the quantitative results of the above-mentioned deep learning-based calibrated (marked as red) and uncalibrated (marked as green) photometric stereo methods on the DiLiGenT benchmark data set [25] under all the 96 input images (dense condition). Uncalibrated photometric stereo methods estimate surface normals with unknown lights. All-pixel methods based on max-pooling, such as PS-FCN [23] and CHR-PSN [11], can handle both calibrated and uncalibrated photometric stereo tasks (without input light directions). However, these methods do not explicitly predict the direction and intensity of the lights. To better solve the uncalibrated case, the following methods apply a two-stage strategy, where the direction and intensity of the lights are first predicted from photometric stereo images, and then the predicted lights information and the image are input into the second-stage network to predict surface normals. SDPS-Net [24] is the first to propose the two-stage deep learning architecture to reduce learning difficulty compared with the single-stage method [23]. UPS-GCNet [72] further utilizes object shape and shading information as guidance for better lighting estimation. Similarly, ReDDLE-Net [73] employs diffuse and specular clues for improving the light estimation, and Sarno *et al.* [77] introduced the Neural Architecture Search (NAS) in the light calibration network and the normal estimation Network. Unlike the above methods, LERPS [82] designed an image relighting network to help learn the estimation using estimated surface

TABLE 3

Performance on the DiLiGenT benchmark [25] with 96 images, in terms of MAE (degrees). The compared methods are ranked by the average MAE of ten objects. Red, green, and blue colors represent the calibrated deep learning methods, uncalibrated deep learning methods, and non-learning calibrated methods, respectively.

Method	Ball	Bear	Bear-76	Buddha	Cat	Cow	Goblet	Harvest	Pot1	Pot2	Reading	Avg.
Baseline [16]	4.10	8.39	-	14.92	8.41	25.60	18.50	30.62	8.89	14.65	19.80	15.39
IW12 [21]	2.54	7.32	-	11.11	7.21	25.70	16.25	29.26	7.74	14.09	16.17	13.74
WG10 [20]	2.06	6.50	-	10.91	6.73	25.89	15.70	30.01	7.18	13.12	15.39	13.35
HM10 [19]	3.55	11.48	-	13.05	8.40	14.95	14.89	21.79	10.85	16.37	16.82	13.22
KS21 [56]	3.78	5.96	-	13.14	7.91	10.85	11.94	25.49	8.75	10.17	18.22	11.62
IA14 [18]	3.34	7.11	-	10.47	6.74	13.05	9.71	25.95	6.64	8.77	14.19	10.60
ST14 [29]	1.74	6.12	-	10.60	6.12	13.93	10.09	25.44	6.51	8.78	13.63	10.30
SPLINE-Net† [34]	4.51	5.28	-	10.36	6.49	7.44	9.62	17.93	8.29	10.89	15.50	9.63
SDPS-Net [24]	2.77	6.89	-	8.97	8.06	8.48	11.91	17.43	8.14	7.50	14.90	9.51
DPSN [22]	2.02	6.31	-	12.68	6.54	8.01	11.28	16.86	7.05	7.86	15.51	9.41
SK22 [77]	3.46	5.48	-	10.00	8.94	6.04	9.78	17.97	7.76	7.10	15.02	9.15
IRPS [35]	1.47	5.79	-	10.36	5.44	6.32	11.47	22.59	6.09	7.76	11.03	8.83
UPS-GCNet [72]	2.50	5.60	-	8.60	7.80	8.48	9.60	16.20	7.20	7.10	14.90	8.70
LMPS [33]	2.40	5.23	-	9.89	6.11	7.98	8.61	16.18	6.54	7.48	13.68	8.41
PS-FCN [23]	2.82	7.55	-	7.91	6.16	7.33	8.60	15.85	7.13	7.25	13.33	8.39
ReDDLE-Net [73]	2.65	6.04	-	7.28	8.76	6.80	8.42	12.28	7.82	7.99	14.03	8.21
Manifold-PSN [44]	3.05	6.31	-	7.39	6.22	7.34	8.85	15.01	7.07	7.01	12.65	8.09
LERPS [82]	2.41	6.93	-	8.84	7.43	6.36	8.78	11.57	8.32	7.01	11.51	7.92
Attention-PSN [36]	2.93	4.86	-	7.75	6.14	6.86	8.42	15.44	6.92	6.97	12.90	7.92
DR-PSN [43]	2.27	5.46	-	7.84	5.42	7.01	8.49	15.40	7.08	7.21	12.74	7.90
GPS-Net [42]	2.92	5.07	-	7.77	5.42	6.14	9.00	15.14	6.04	7.01	13.58	7.81
JJ21 [13]	2.51	5.77	-	7.88	6.56	6.29	8.40	14.95	7.21	7.40	11.01	7.80
CHR-PSN [11]	2.26	6.35	-	7.15	5.97	6.05	8.32	15.32	7.04	6.76	12.52	7.77
CNN-PS† [32]	2.12	8.30	4.10	8.07	4.38	7.92	7.42	14.08	5.37	6.38	12.12	7.62
SPS-Net [61]	2.80	-	-	6.90	5.10	6.30	7.10	13.70	7.50	7.40	11.90	7.60
MT-PS-CNN [55]	2.29	5.79	-	6.85	5.87	7.48	7.88	13.71	6.92	6.89	11.94	7.56
HS17 [31]	1.33	5.58	-	8.48	4.88	8.23	7.57	15.81	5.16	6.41	12.08	7.55
PS-FCN (Norm.) [47]	2.67	7.72	-	7.53	4.76	6.72	7.84	12.39	6.17	7.15	10.92	7.39
MF-PSN [10]	2.07	5.83	-	6.88	5.00	5.90	7.46	13.38	7.20	12.20	12.20	7.27
LL22b [83]	1.24	3.82	-	9.28	4.72	5.53	7.12	14.96	6.73	6.50	10.54	7.05
HT21† [12]	2.49	8.96	3.59	7.23	4.69	4.89	6.89	12.79	5.10	4.98	11.08	6.91
NormAttention-PSN [50]	2.93	5.48	4.80	7.12	4.65	5.99	7.49	12.28	5.96	6.42	9.93	6.83
WZ20 [37]	1.78	5.26	4.12	6.09	4.66	6.33	7.22	13.34	6.46	6.45	10.05	6.76
LL22a [59]	2.43	-	3.64	8.04	4.86	4.72	6.68	14.90	5.99	4.97	8.75	6.50
PX-Net† [9]	2.03	4.13	3.57	7.61	4.39	4.69	6.90	13.10	5.08	5.10	10.26	6.33

normals and lights, which is similar to DR-PSN [43]. Li *et al.* [83] proposed a neural inverse rendering network to render objects by considering the lighting, surface normal, diffuse albedo, and specular components, where the specularities are used to solve the uncalibrated problem.

Besides deep learning methods, we also evaluate the performance of some representative non-learning-based calibrated algorithms (marked as blue) and compare them with deep learning-based methods. As shown in Table 3, for most of the learning-based methods, they are represented by their networks’ names. For non-learning methods and some learning-based methods without given names, we present them by the first letter of the authors’ name and the published year. We also use † to represent the networks trained by CyclePS [32] rendered by Disney’s principled BSDFs [15]. Furthermore, some recent models discarded the first 20 images of “Bear” in testing (*i.e.*, tested with the remaining 76 images) because the first 20 images are photometrically inconsistent in the belly region [32]. For these methods, we tabulate both the results of “Bear” input with 76 images and 96 images, denoted as “Bear-76”

(marked with yellow) and “Bear”, respectively. For a fair comparison, the average MAE of these ten objects uses the result of “Bear” rather than “Bear-76”. Since parallel white lights were used in the DiLiGenT benchmark [25], we can only evaluate the methods for calibrated and un-calibrated photometric stereos, ignoring methods for near-field light, general light, and color light.

Similarly, we review the performance of these calibrated deep learning-based photometric stereo methods in the sparse condition (10 input images) tabulated in Table 4. Note that not all the methods report the results under 10 input images, and some methods only provide the sparse condition without dense input, such as PS-Transform [62].

As displayed in Tables 3 and 4, the results based on deep learning-based photometric methods generally achieve better performance, as compared with non-learning methods, especially in objects with complex structure (“Buddha”, “Harvest”, “Reading”) and strong non-Lambertian reflectance (“Cow”, “Goblet”, “Reading”). This illustrates the capability and generalization of deep learning techniques. However, it can be seen that most deep learning models



TABLE 4

Performance on the DiLiGenT benchmark [25] with 10 images, in terms of MAE (degrees). The compared methods are ranked by the average MAE of ten objects. Red and green colors represent the calibrated deep learning methods and uncalibrated deep learning methods, respectively.

Method	Ball	Bear	Buddha	Cat	Cow	Goblet	Harvest	Pot1	Pot2	Reading	Avg.
IA14 [18]	12.94	16.40	20.63	15.53	18.08	18.73	32.50	6.28	14.31	24.99	19.04
Baseline [16]	5.09	11.59	16.25	9.66	27.90	19.97	33.41	11.32	18.03	19.86	17.31
ST14 [29]	5.24	9.39	15.79	9.34	26.08	19.71	30.85	9.76	15.57	20.08	16.18
IW12 [21]	3.33	7.62	13.36	8.13	25.01	18.01	29.37	8.73	14.60	16.63	14.48
CNN-PS† [32]	9.11	14.08	14.58	11.71	14.04	15.48	19.56	13.23	14.65	16.99	14.34
IRPS [35]	2.12	6.92	11.41	6.58	8.87	14.99	26.55	7.14	9.61	13.70	10.79
PS-FCN [23]	4.02	7.18	9.79	8.80	10.51	11.58	18.70	10.14	9.85	15.03	10.51
SPLINE-Net† [34]	4.96	5.99	10.07	7.52	8.80	10.43	19.05	8.77	11.79	16.13	10.35
PS-FCN (Norm.) [47]	4.38	5.92	8.98	6.30	14.66	10.96	18.04	7.05	11.91	13.23	10.14
LMPS [33]	3.97	8.73	11.36	6.69	10.19	10.46	17.33	7.30	9.74	14.37	10.02
DR-PSN [43]	3.83	7.52	9.55	7.92	9.83	10.38	17.12	9.36	9.16	14.75	9.94
CHR-PSN [11]	3.91	7.84	9.59	8.10	8.54	10.36	17.21	9.65	9.61	14.35	9.92
MT-PS-CNN [55]	4.20	8.59	8.25	7.30	10.84	10.44	16.97	8.78	9.85	13.17	9.84
JJ21 [13]	3.86	7.49	9.69	7.82	8.55	10.31	16.94	9.28	9.54	14.30	9.78
GPS-Net [42]	4.33	6.34	8.87	6.81	9.34	10.79	16.92	7.50	8.38	15.00	9.43
SPS-Net [42]	4.60	-	8.00	6.90	8.30	9.00	16.70	8.90	9.00	13.60	9.40
MF-PSN [10]	2.97	4.89	7.43	5.55	8.41	9.87	12.92	7.21	9.16	12.92	8.48
PX-Net† [9]	2.50	4.90	9.40	6.30	7.20	9.70	16.10	7.00	7.70	13.10	8.37
WJ20 [37]	2.30	5.18	7.05	5.62	7.53	8.80	15.26	7.08	8.19	10.88	7.79
PS-Transformer† [62]	3.27	4.88	8.65	5.34	6.54	9.28	14.41	6.06	6.97	11.24	7.66

achieve ordinary performance on very simple objects with almost diffuse reflectance, such as “Ball”. We believe that this may result from overfitting in “complex” network structures and “difficult” BRDF training data sets [15], [40] that pay more attention to non-Lambertian materials [34].

## 8 FUTURE TRENDS

In this section, we point out some promising trends for future development, based on the discussion in the above sections. First, we focus on the problem of calibrated photometric stereo. Then, we raise the perspective to the entire photometric stereo community.

As discussed in Section 3, we compare the unique characteristics of per-pixel and all-pixel methods. These methods can be further explored and better combined. For per-pixel methods, we believe that some further developments can be found in observation maps [32], *e.g.*, how to optimize unstructured light vectors via a graph-based network [84] in the “observation map”, how to embed the information from adjacent surface points in a per-pixel manner. For all-pixel methods, we believe that the fusion of inter-images (inter-patches) still needs to be improved. Existing methods apply max-pooling [10], [23], [50] or manifold learning [44] to aggregate a flexible number of input images. However, these methods are underutilized for fusing features or suffer from cumbersome training pipelines. Therefore, a better fusion strategy should be proposed, which can leverage the self-attention mechanism [60] to learn the weights of input features. Of course, a more far-sighted research direction is how to efficiently combine per-pixel and all-pixel methods, which has been initially discussed in recent combined works [12], [55], and can be further explored by mutually combining with more physical cues. Furthermore, we argue that deep learning photometric stereo models can be further

improved by excavating prior knowledge [13], [37] and supervisions [45], [82].

In fact, many deep learning-based photometric stereo methods discussed above are calibrated photometric stereo algorithms, which assume stringent requirements, such as accurate directions of incident illuminations, distant (parallel) illuminations, and standard darkrooms, *etc.* In practical applications, almost all assumptions are not satisfied. When reviewing the realistic environment, we naturally expect a general or universal model that can handle un-calibrated light [24], [72], [73], [77], [83], the colored light [45], [46], [85], the near-field light [74], [75], [76], the general light [78], and even a perspective projection camera simultaneously. Recently, an inspiring work UniPS [79] first drops the physical lighting models and extracts a generic lighting representation in image interaction. In this way, UniPS can handle arbitrary lighting variations, such as parallel lighting, spatially-varying lighting, near-filed lighting, and outdoor wild lighting. However, a deeper analysis of global lighting contexts is missing. Along this direction, we believe that more works can explore the extraction of global lighting, and the ensemble learning framework may be considered to handle multiple light conditions.

## 9 CONCLUSION

In this paper, we conducted a systematic review of deep learning-based photometric stereo methods. According to our taxonomy focusing on calibrated deep learning-based photometric stereo methods, we have summarized and discussed the strengths and weaknesses of these models by categorizing them by input processing, supervision, and network architecture. We also introduce the used training data sets and test benchmarks in the field of photometric stereo. Then, more than thirty calibrated and uncalibrated deep

learning models for photometric stereo are evaluated on the widely used benchmark. Compared with traditional non-learning methods, deep learning-based photometric stereo models are superior in estimating surface normals. Finally, we point out the future trends in the field of photometric stereo. We hope that this survey will help researchers to orient themselves to develop in this growing field, as well as highlight opportunities for future research.

## REFERENCES

- [1] Yuji Iwahori, Robert J Woodham, Hidekazu Tanaka, and Naohiro Ishii, "Neural network to reconstruct specular surface shape from its three shading images," in *Proceedings of the International Conference on Neural Networks*, 1993, vol. 2, pp. 1181–1184.
- [2] Wen-Chang Cheng, "Neural-network-based photometric stereo for 3d surface reconstruction," in *Proceedings of the International Joint Conference on Neural Network*, 2006, pp. 404–410.
- [3] Zhenglong Zhou, Zhe Wu, and Ping Tan, "Multi-view photometric stereo with spatially varying isotropic materials," in *Proceedings of the IEEE Conference on Computer Vision and Pattern Recognition*, 2013, pp. 1482–1489.
- [4] Hao Fan, Lin Qi, Yakun Ju, Junyu Dong, and Hui Yu, "Refractive laser triangulation and photometric stereo in underwater environment," *Optical Engineering*, vol. 56, no. 11, pp. 113101, 2017.
- [5] Bo Wu, Yuan Li, Wai Chung Liu, Yiran Wang, Fei Li, Yang Zhao, and He Zhang, "Centimeter-resolution topographic modeling and fine-scale analysis of craters and rocks at the chang'e-4 landing site," *Earth and Planetary Science Letters*, vol. 553, pp. 116666, 2021.
- [6] Mingjun Ren, Xi Wang, Gaobo Xiao, Minghan Chen, and Lin Fu, "Fast defect inspection based on data-driven photometric stereo," *IEEE Transactions on Instrumentation and Measurement*, vol. 68, no. 4, pp. 1148–1156, 2018.
- [7] David Elizondo, Shang-Ming Zhou, and Charalambos Chrysostomou, "Surface reconstruction techniques using neural networks to recover noisy 3d scenes," in *Proceedings of the International Conference on Artificial Neural Networks*, 2008, pp. 857–866.
- [8] Qian Zheng, Boxin Shi, and Gang Pan, "Summary study of data-driven photometric stereo methods," *Virtual Reality and Intelligent Hardware*, vol. 2, no. 3, pp. 213–221, 2020.
- [9] Fotios Logothetis, Ignas Budvytis, Roberto Mecca, and Roberto Cipolla, "Px-net: Simple and efficient pixel-wise training of photometric stereo networks," in *Proceedings of the International Conference on Computer Vision*, 2021, pp. 12757–12766.
- [10] Yanru Liu, Yakun Ju, Muwei Jian, Feng Gao, Yuan Rao, Yeqi Hu, and Junyu Dong, "A deep-shallow and global-local multi-feature fusion network for photometric stereo," *Image and Vision Computing*, vol. 118, pp. 104368, 2022.
- [11] Yakun Ju, Yuxin Peng, Muwei Jian, Feng Gao, and Junyu Dong, "Learning conditional photometric stereo with high-resolution features," *Computational Visual Media*, vol. 8, no. 1, pp. 105–118, 2022.
- [12] David Honzátka, Engin Türetken, Pascal Fua, and L Andrea Dunbar, "Leveraging spatial and photometric context for calibrated non-lambertian photometric stereo," in *Proceedings of the International Conference on 3D Vision*, 2021, pp. 394–402.
- [13] Yakun Ju, Muwei Jian, Shaoxiang Guo, Yingyu Wang, Huiyu Zhou, and Junyu Dong, "Incorporating lambertian priors into surface normals measurement," *IEEE Transactions on Instrumentation and Measurement*, vol. 70, pp. 1–13, 2021.
- [14] Gao Huang, Zhuang Liu, Laurens Van Der Maaten, and Kilian Q Weinberger, "Densely connected convolutional networks," in *Proceedings of the Conference on Computer Vision and Pattern Recognition*, 2017, pp. 4700–4708.
- [15] Stephen McAuley, Stephen Hill, Naty Hoffman, Yoshiharu Gotanda, Brian Smits, Brent Burley, and Adam Martinez, "Practical physically-based shading in film and game production," in *ACM SIGGRAPH 2012 Courses*, pp. 1–7, 2012.
- [16] R. J Woodham, "Photometric method for determining surface orientation from multiple images," *Optical Engineering*, vol. 19, no. 1, pp. 139–144, 1980.
- [17] Neil Alldrin, Todd Zickler, and David Kriegman, "Photometric stereo with non-parametric and spatially-varying reflectance," in *Proceedings of the IEEE Conference on Computer Vision and Pattern Recognition*. IEEE, 2008, pp. 1–8.
- [18] Satoshi Ikehata and Kiyoharu Aizawa, "Photometric stereo using constrained bivariate regression for general isotropic surfaces," in *Proceedings of the IEEE Conference on Computer Vision and Pattern Recognition*, 2014, pp. 2179–2186.
- [19] Tomoaki Higo, Yasuyuki Matsushita, and Katsushi Ikeuchi, "Consensus photometric stereo," in *Proceedings of the IEEE Conference on Computer Vision and Pattern Recognition*, 2010, pp. 1157–1164.
- [20] Lun Wu, Arvind Ganesh, Boxin Shi, Yasuyuki Matsushita, Yongtian Wang, and Yi Ma, "Robust photometric stereo via low-rank matrix completion and recovery," in *Proceedings of the Asian Conference on Computer Vision*, 2010, pp. 703–717.
- [21] Satoshi Ikehata, David Wipf, Yasuyuki Matsushita, and Kiyoharu Aizawa, "Robust photometric stereo using sparse regression," in *Proceedings of the IEEE Conference on Computer Vision and Pattern Recognition*, 2012, pp. 318–325.
- [22] Hiroaki Santo, Masaki Samejima, Yusuke Sugano, Boxin Shi, and Yasuyuki Matsushita, "Deep photometric stereo network," in *Proceedings of the IEEE International Conference on Computer Vision Workshops*, 2017, pp. 501–509.
- [23] Guanying Chen, Kai Han, and Kwan-Yee K Wong, "Ps-fcn: A flexible learning framework for photometric stereo," in *Proceedings of the European Conference on Computer Vision*, 2018, pp. 3–18.
- [24] Guanying Chen, Kai Han, Boxin Shi, Yasuyuki Matsushita, and Kwan-Yee K Wong, "Self-calibrating deep photometric stereo networks," in *Proceedings of the IEEE Conference on Computer Vision and Pattern Recognition*, 2019, pp. 8739–8747.
- [25] B Shi, Z Mo, Z Wu, D Duan, SK Yeung, and P Tan, "A benchmark dataset and evaluation for non-lambertian and uncalibrated photometric stereo," *IEEE Transactions on Pattern Analysis and Machine Intelligence*, vol. 41, no. 2, pp. 271–284, 2019.
- [26] Shree K Nayar, Katsushi Ikeuchi, and Takeo Kanade, "Shape from interreflections," *International Journal of Computer Vision*, vol. 6, no. 3, pp. 173–195, 1991.
- [27] Steffen Herbot and Christian Wöhler, "An introduction to image-based 3d surface reconstruction and a survey of photometric stereo methods," *3D Research*, vol. 2, no. 3, pp. 4, 2011.
- [28] Dan B Goldman, Brian Curless, Aaron Hertzmann, and Steven M Seitz, "Shape and spatially-varying brdfs from photometric stereo," *IEEE Transactions on Pattern Analysis and Machine Intelligence*, vol. 32, no. 6, pp. 1060–1071, 2009.
- [29] Boxin Shi, Ping Tan, Yasuyuki Matsushita, and Katsushi Ikeuchi, "Bi-polynomial modeling of low-frequency reflectances," *IEEE Transactions on Pattern Analysis and Machine Intelligence*, , no. 6, pp. 1078–1091, 2014.
- [30] Aaron Hertzmann and Steven M Seitz, "Example-based photometric stereo: Shape reconstruction with general, varying brdfs," *IEEE Transactions on Pattern Analysis and Machine Intelligence*, vol. 27, no. 8, pp. 1254–1264, 2005.
- [31] Zhuo Hui and Aswin C Sankaranarayanan, "Shape and spatially-varying reflectance estimation from virtual exemplars," *IEEE Transactions on Pattern Analysis and Machine Intelligence*, vol. 39, no. 10, pp. 2060–2073, 2016.
- [32] Satoshi Ikehata, "Cnn-ps: Cnn-based photometric stereo for general non-convex surfaces," in *Proceedings of the European Conference on Computer Vision*, 2018, pp. 3–18.
- [33] Junxuan Li, Antonio Robles-Kelly, Shaodi You, and Yasuyuki Matsushita, "Learning to minify photometric stereo," in *Proceedings of the IEEE Conference on Computer Vision and Pattern Recognition*, 2019, pp. 7568–7576.
- [34] Qian Zheng, Yiming Jia, Boxin Shi, Xudong Jiang, Ling-Yu Duan, and Alex C Kot, "Spline-net: Sparse photometric stereo through lighting interpolation and normal estimation networks," in *Proceedings of the IEEE International Conference on Computer Vision*, 2019, pp. 8549–8558.
- [35] Tatsunori Tani and Takanori Maehara, "Neural inverse rendering for general reflectance photometric stereo," in *Proceedings of the International Conference on Machine Learning*, 2018, pp. 4857–4866.
- [36] Yakun Ju, Kin-Man Lam, Yang Chen, Lin Qi, and Junyu Dong, "Pay attention to devils: A photometric stereo network for better details," in *Proceedings of the International Joint Conference on Artificial Intelligence*, 2020, pp. 694–700.
- [37] Xi Wang, Zhenxiong Jian, and Mingjun Ren, "Non-lambertian photometric stereo network based on inverse reflectance model with collocated light," *IEEE Transactions on Image Processing*, vol. 29, pp. 6032–6042, 2020.
- [38] Kaiming He, Xiangyu Zhang, Shaoqing Ren, and Jian Sun, "Deep

- residual learning for image recognition," in *Proceedings of the IEEE International Conference on Computer Vision*, 2016, pp. 770–778.
- [39] Micah K Johnson and Edward H Adelson, "Shape estimation in natural illumination," in *Proceedings of the IEEE International Conference on Computer Vision*, 2011, pp. 2553–2560.
- [40] Wojciech Matusik, Hanspeter Pfister, Matt Brand, and Leonard McMillan, "A data-driven reflectance model," *ACM Transactions on Graphics*, vol. 22, no. 3, pp. 759–769, 2003.
- [41] Wenzel Jakob, "Mitsuba renderer," 2010.
- [42] Zhuokun Yao, Kun Li, Ying Fu, Haofeng Hu, and Boxin Shi, "Gps-net: Graph-based photometric stereo network," in *Proceedings of Advances in Neural Information Processing Systems*, 2020, p. 33.
- [43] Yakun Ju, Junyu Dong, and Sheng Chen, "Recovering surface normal and arbitrary images: A dual regression network for photometric stereo," *IEEE Transactions on Image Processing*, vol. 30, pp. 3676–3690, 2021.
- [44] Yakun Ju, Muwei Jian, Junyu Dong, and Kin-Man Lam, "Learning photometric stereo via manifold-based mapping," in *2020 IEEE International Conference on Visual Communications and Image Processing*, 2020, pp. 411–414.
- [45] Yakun Ju, Xinghui Dong, Yingyu Wang, Lin Qi, and Junyu Dong, "A dual-cue network for multispectral photometric stereo," *Pattern Recognition*, vol. 100, pp. 107162, 2020.
- [46] Yakun Ju, Lin Qi, Jichao He, Xinghui Dong, Feng Gao, and Junyu Dong, "Mps-net: Learning to recover surface normal for multispectral photometric stereo," *Neurocomputing*, vol. 375, pp. 62–70, 2020.
- [47] Guanying Chen, Kai Han, Boxin Shi, Yasuyuki Matsushita, and Kwan-Yee Kenneth Wong, "Deep photometric stereo for non-lambertian surfaces," *IEEE Transactions on Pattern Analysis and Machine Intelligence*, vol. 44, no. 1, pp. 129–142, 2020.
- [48] Ke Sun, Bin Xiao, Dong Liu, and Jingdong Wang, "Deep high-resolution representation learning for human pose estimation," in *Proceedings of the IEEE Conference on Computer Vision and Pattern Recognition*, 2019, pp. 5693–5703.
- [49] Olivia Wiles and Andrew Zisserman, "Silnet: Single-and multi-view reconstruction by learning from silhouettes," in *Proceedings of the British Machine Vision Conference*, 2017, pp. 99.1–99.13.
- [50] Yakun Ju, Boxin Shi, Muwei Jian, Lin Qi, Junyu Dong, and Kin-Man Lam, "Normattention-psn: A high-frequency region enhanced photometric stereo network with normalized attention," *International Journal of Computer Vision*, 2022.
- [51] Wilfried Hartmann, Silvano Galliani, Michal Havlena, Luc Van Gool, and Konrad Schindler, "Learned multi-patch similarity," in *Proceedings of the International Conference on Computer Vision*, 2017, pp. 1586–1594.
- [52] Alex Graves, Abdel-rahman Mohamed, and Geoffrey Hinton, "Speech recognition with deep recurrent neural networks," in *Proceedings of the International Conference on Acoustics, Speech and Signal Processing*, 2013, pp. 6645–6649.
- [53] Phillip Isola, Jun-Yan Zhu, Tinghui Zhou, and Alexei A Efros, "Image-to-image translation with conditional adversarial networks," in *Proceedings of the Conference on Computer Vision and Pattern Recognition*, 2017, pp. 1125–1134.
- [54] Euijeong Song and Minh Chang, "Photometric stereo using cnn-based feature-merging network," in *Proceedings of the International Conference on Control, Automation and Systems*, 2020, pp. 865–868.
- [55] Yanlong Cao, Binjie Ding, Zewei He, Jiangxin Yang, Jingxi Chen, Yanpeng Cao, and Xin Li, "Learning inter-and intraframe representations for non-lambertian photometric stereo," *Optics and Lasers in Engineering*, vol. 150, pp. 106838, 2022.
- [56] Berk Kaya, Suryansh Kumar, Carlos Oliveira, Vittorio Ferrari, and Luc Van Gool, "Uncalibrated neural inverse rendering for photometric stereo of general surfaces," in *Proceedings of the IEEE Conference on Computer Vision and Pattern Recognition*, 2021, pp. 3804–3814.
- [57] Hiroaki Santo, Masaki Samejima, Yusuke Sugano, Boxin Shi, and Yasuyuki Matsushita, "Deep photometric stereo networks for determining surface normal and reflectances," *IEEE Transactions on Pattern Analysis and Machine Intelligence*, vol. 44, no. 01, pp. 114–128, 2022.
- [58] Jieji Ren, Feishi Wang, Jiahao Zhang, Qian Zheng, Mingjun Ren, and Boxin Shi, "Diligent102: A photometric stereo benchmark dataset with controlled shape and material variation," in *Proceedings of the IEEE Conference on Computer Vision and Pattern Recognition*, 2022, pp. 12581–12590.
- [59] Junxuan Li and Hongdong Li, "Neural reflectance for shape recovery with shadow handling," in *Proceedings of the IEEE Conference on Computer Vision and Pattern Recognition*, 2022, pp. 16221–16230.
- [60] Ashish Vaswani, Noam Shazeer, Niki Parmar, Jakob Uszkoreit, Llion Jones, Aidan N Gomez, Łukasz Kaiser, and Illia Polosukhin, "Attention is all you need," in *Proceedings of the Advances in Neural Information Processing Systems*, 2017.
- [61] Huiyu Liu, Yunhui Yan, Kechen Song, and Han Yu, "Sps-net: Self-attention photometric stereo network," *IEEE Transactions on Instrumentation and Measurement*, vol. 70, pp. 1–13, 2020.
- [62] Satoshi Ikehata, "Ps-transformer: Learning sparse photometric stereo network using self-attention mechanism," in *Proceedings of the British Machine Vision Conference*, 2021, vol. 2, p. 11.
- [63] Gedas Bertasius, Heng Wang, and Lorenzo Torresani, "Is space-time attention all you need for video understanding?," in *Proceedings of the International Conference on Machine Learning*, 2021, vol. 2, p. 4.
- [64] Robin Strudel, Ricardo Garcia, Ivan Laptev, and Cordelia Schmid, "Segformer: Transformer for semantic segmentation," in *Proceedings of the IEEE International Conference on Computer Vision*, 2021, pp. 7262–7272.
- [65] Rasmus Jensen, Anders Dahl, George Vogiatzis, Engin Tola, and Henrik Aanæs, "Large scale multi-view stereopsis evaluation," in *Proceedings of the IEEE Conference on Computer Vision and Pattern Recognition*, 2014, pp. 406–413.
- [66] Angel X Chang, Thomas Funkhouser, Leonidas Guibas, Pat Hanrahan, Qixing Huang, Zimo Li, Silvio Savarese, Manolis Savva, Shuran Song, Hao Su, et al., "Shapenet: An information-rich 3d model repository," *arXiv preprint arXiv:1512.03012*, 2015.
- [67] Henrik Aanæs, Rasmus Ramsbøl Jensen, George Vogiatzis, Engin Tola, and Anders Bjorholm Dahl, "Large-scale data for multiple-view stereopsis," *International Journal of Computer Vision*, vol. 120, no. 2, pp. 153–168, 2016.
- [68] Tai-Pang Wu and Chi-Keung Tang, "Photometric stereo via expectation maximization," *IEEE Transactions on Pattern Analysis and Machine Intelligence*, vol. 32, no. 3, pp. 546–560, 2009.
- [69] Bernardo Iraci, *Blender cycles: Lighting and rendering cookbook*, Packt Publishing Ltd, 2013.
- [70] Brian Curless and Marc Levoy, "A volumetric method for building complex models from range images," in *Proceedings of the Annual Conference on Computer Graphics and Interactive Techniques*, 1996, pp. 303–312.
- [71] Massimiliano Corsini, Matteo Dellepiane, Federico Ponchio, and Roberto Scopigno, "Image-to-geometry registration: A mutual information method exploiting illumination-related geometric properties," in *Computer Graphics Forum*, 2009, vol. 28, pp. 1755–1764.
- [72] Guanying Chen, Michael Waechter, Boxin Shi, Kwan-Yee K Wong, and Yasuyuki Matsushita, "What is learned in deep uncalibrated photometric stereo?," in *Proceedings of the European conference on computer vision*, 2020, pp. 745–762.
- [73] Jiangxin Yang, Binjie Ding, Zewei He, Gang Pan, Yanpeng Cao, Yanlong Cao, and Qian Zheng, "Reddle-net: Reflectance decomposition for directional light estimation," in *Photonics*, 2022, vol. 9, p. 656.
- [74] Fotios Logothetis, Roberto Mecca, Ignas Budvytis, and Roberto Cipolla, "A cnn based approach for the point-light photometric stereo problem," *International Journal of Computer Vision*, pp. 1–20, 2022.
- [75] Hiroaki Santo, Michael Waechter, and Yasuyuki Matsushita, "Deep near-light photometric stereo for spatially varying reflectances," in *European Conference on Computer Vision*, 2020, pp. 137–152.
- [76] Heng Guo, Hiroaki Santo, Boxin Shi, and Yasuyuki Matsushita, "Edge-preserving near-light photometric stereo with neural surfaces," *arXiv preprint arXiv:2207.04622*, 2022.
- [77] Francesco Sarno, Suryansh Kumar, Berk Kaya, Zhiwu Huang, Vittorio Ferrari, and Luc Van Gool, "Neural architecture search for efficient uncalibrated deep photometric stereo," in *Proceedings of the IEEE Winter Conference on Applications of Computer Vision*, 2022, pp. 361–371.
- [78] Yannick Hold-Geoffroy, Paulo Gotardo, and Jean-François Lalonde, "Single day outdoor photometric stereo," *IEEE Transactions on Pattern Analysis and Machine Intelligence*, vol. 43, no. 6, pp. 2062–2074, 2019.
- [79] Satoshi Ikehata, "Universal photometric stereo network using global lighting contexts," in *Proceedings of the IEEE Conference on Computer Vision and Pattern Recognition*, 2022, pp. 12591–12600.

- [80] Yakun Ju, Lin Qi, Huiyu Zhou, Junyu Dong, and Liang Lu, "Demultiplexing colored images for multispectral photometric stereo via deep neural networks," *IEEE Access*, vol. 6, pp. 30804–30818, 2018.
- [81] Wenqi Yang, Guanying Chen, Chaofeng Chen, Zhenfang Chen, and Kwan-Yee K Wong, "Ps-nerf: Neural inverse rendering for multi-view photometric stereo," in *Proceedings of the European Conference on Computer Vision*, 2022, pp. 266–284.
- [82] Ashish Tiwari and Shanmuganathan Raman, "Lerps: Lighting estimation and relighting for photometric stereo," in *Proceedings of the IEEE International Conference on Acoustics, Speech and Signal Processing*, 2022, pp. 2060–2064.
- [83] Junxuan Li and Hongdong Li, "Self-calibrating photometric stereo by neural inverse rendering," in *Proceedings of the European Conference on Computer Vision*, 2022.
- [84] Felix Wu, Amauri Souza, Tianyi Zhang, Christopher Fifty, Tao Yu, and Kilian Weinberger, "Simplifying graph convolutional networks," in *Proceedings of the International Conference on Machine Learning*, 2019, pp. 6861–6871.
- [85] Doris Antensteiner, Svorad Stolc, and Daniel Soukup, "Single image multi-spectral photometric stereo using a split u-shaped cnn," in *Proceedings of the IEEE Conference on Computer Vision and Pattern Recognition Workshops*, 2019.
- [86] Min Li, Zhenglong Zhou, Zhe Wu, Boxin Shi, Changyu Diao, and Ping Tan, "Multi-view photometric stereo: A robust solution and benchmark dataset for spatially varying isotropic materials," *IEEE Transactions on Image Processing*, vol. 29, pp. 4159–4173, 2020.
- [87] Roberto Mecca, Fotios Logothetis, Ignas Budvytis, and Roberto Cipolla, "Lucas: A dataset for near-field point light source photometric stereo," *arXiv preprint arXiv:2104.13135*, 2021.
- [88] Jianlong Chang, Jie Gu, Lingfeng Wang, Gaofeng Meng, Shiming Xiang, and Chunhong Pan, "Structure-aware convolutional neural networks," in *Proceedings of the International Conference on Neural Information Processing Systems*, 2018, pp. 11–20.
- [89] Juho Lee, Yoonho Lee, Jungtaek Kim, Adam Kosiorek, Seungjin Choi, and Yee Whye Teh, "Set transformer: A framework for attention-based permutation-invariant neural networks," in *International conference on machine learning*, 2019, pp. 3744–3753.
- [90] Joshua B Tenenbaum, Vin de Silva, and John C Langford, "A global geometric framework for nonlinear dimensionality reduction," *science*, vol. 290, no. 5500, pp. 2319–2323, 2000.